

Role of the orbital degree of freedom in iron-based superconductors

Ming Yi^{1,2†}, Yan Zhang^{1,3†}, Zhi-Xun Shen^{1,2*}, and Donghui Lu^{4*}

¹*Stanford Institute for Materials and Energy Sciences, SLAC National Accelerator Laboratory
and Stanford University, Menlo Park, California 94025, USA*

²*Departments of Physics and Applied Physics, and Geballe Laboratory for Advanced Materials,
Stanford University, Stanford, California 94305, USA*

³*Advanced Light Source, Lawrence Berkeley National Lab, Berkeley, California 94720, USA*

⁴*Stanford Synchrotron Radiation Lightsource, SLAC National Accelerator Laboratory, Menlo
Park, California 94025, USA*

[†]*These authors contributed equally*

**To whom correspondence should be addressed: dhlu@slac.stanford.edu and
zxshen@stanford.edu*

Abstract

Almost a decade has passed since the serendipitous discovery of the iron-based high temperature superconductors (FeSCs) in 2008. The fact that, as in the copper oxide high temperature superconductors, long-range antiferromagnetism in the FeSCs arises in proximity to superconductivity immediately raised the question of the degree of similarity between the two. Despite the great resemblance in their phase diagrams, there exist important differences between the FeSCs and the cuprates that need to be considered in order to paint a full picture of these two families of high temperature superconductors. One of the key differences is the multi-orbital multi-band nature of the FeSCs, which contrasts with the effective single-band nature of the cuprates. Systematic studies of orbital related phenomena in FeSCs have been largely lacking. In this review, we summarize angle-resolved photoemission spectroscopy (ARPES) measurements across various FeSC families that have been reported in literature, focusing on the systematic trends of orbital dependent electron correlations and the role of different Fe 3d orbitals in driving the nematic transition, the spin-density-wave transition, and superconductivity.

Introduction

Thirty years after the historic discovery of cuprate high temperature superconductors, the mechanism for high temperature superconductivity remains the biggest challenge in condensed matter physics despite tremendous amount of theoretical and experimental efforts. The discovery of iron-based superconductors¹ provides a great opportunity to identify the important ingredients

that are common to both families of high T_c materials and to test the theoretical models that have been formulated for cuprates. Comparing FeSCs with cuprates, the most striking similarity is the common phase diagram, in which unconventional superconductivity appears in the vicinity of other competing phases, such as the pseudogap phase and the charge order in cuprates and the spin-density-wave (SDW) phase and nematic phase in FeSCs²⁻³. The emergence of superconductivity always takes place with the suppression of these competing phases. Such a remarkable resemblance has raised our hope for a unified theory of high temperature superconductivity and has motivated many theorists to take the strong coupling approach to describe FeSCs.

On the other hand, FeSCs also appear to distinguish themselves from cuprates in various aspects, including metallicity of the parent phase, crystal structure of the conduction layer, spin symmetry of the antiferromagnetic order, as well as the underlying electronic structure. Prior to establishing a unified understanding of the physics in cuprates and FeSCs, we first need to understand whether these differences are trivial nuances or critical ingredients that cannot be neglected. Among them, the most fundamental difference is the multi-orbital multi-band nature of the underlying electronic structure in FeSCs. In contrast to cuprates, for which essential physics seems to take place in a single effective band and Fermi surface, there are at least three out of five Fe 3d orbitals that are active near the Fermi level (E_F) in FeSCs, forming multiple Fermi surface sheets. The complexity of theoretical treatment for a multi-band system has led to various proposals for minimal models for FeSCs, in which the orbital degree of freedom is often

ignored for simplicity. While these models capture some underlying physics, the question is whether they miss important orbital related physics.

The lack of systematic experimental studies on the role of different Fe 3d orbitals may be part of the reason that orbital physics in FeSCs has not garnered as much attention as they perhaps deserved. In this review, we summarize experimental evidence of various orbital dependent phenomena in the electronic structure from angle-resolved photoemission spectroscopy literature. For a recent review on the progress of theoretical studies on the orbital degree of freedom, please see Ref. 4. First, we discuss systematic trends on the normal state electronic structure across different families of FeSCs. In particular, we point out a systematic change of the orbital related physics, for example the increase of orbital-selective electron correlations across the wide spectrum of FeSC compounds based on both structural parameters and charge carrier doping. Eventually, this growth of orbital-dependent correlations naturally culminates in a complete localization of a single orbital while other orbitals remain itinerant—an orbital-selective Mott phase. Hence the orbital degree of freedom plays an important role in balancing the coexistence of local and itinerant physics in the normal state of the FeSCs. We then focus on the manifestations of different Fe 3d orbitals across the nematic and the SDW transitions. In the nematic state, strong anisotropy occurs in the hopping of the d_{xz} , d_{yz} , and d_{xy} orbitals as characterized by a momentum dependent reconstruction of d_{xz} , d_{yz} , and d_{xy} bands. In the SDW state, bands fold and SDW gaps open. The SDW gap is also strongly orbital-dependent. It is large on the d_{xy} bands but moderate on the d_{xz}/d_{yz} bands. These observations have strong

implications on the theories aiming to understand the nature of those competing phases and suggest an important role of multi-orbital nature of FeSCs in driving the nematic and SDW transitions. In the end, we discuss the non-trivial implications of multi-orbital nature on the superconducting pairing mechanism of these materials.

The normal state

All FeSC compounds, regardless of their compositions, share in common planes containing iron and pnictogen (P/As) or chalcogen (S/Se/Te), which is located alternatingly above and below the Fe lattice (Fig. 1a). The difference among FeSC families is the composition and structure of interlayers between the Fe planes. In some cases, these interlayers form charge reservoirs that donate charge carriers to the Fe planes. The normal state is defined as the phase outside the boundaries of the magnetic and structural transitions (Fig. 1a). All FeSC compounds share in common the basic electronic structure consisting of Fe 3d bands near E_F , with the d_{xz} , d_{yz} , and d_{xy} orbitals most active near E_F . The basic electronic structure of FeSC in the normal state is illustrated in Fig. 1c, where three hole-like bands reside near the Brillouin Zone (BZ) center, Γ , and two electron-like bands near the BZ corner, M (except in the case of the 122 structure, where this point is called the X point). For different doping levels and structural subtleties, the overall or relative positions of the hole and electrons bands may vary in energy, leading to different Fermi surface topologies with varying number of hole pockets at Γ and electron pockets at M (Fig. 1d). For undoped parent compounds, the hole pockets at Γ and electron pockets at M are of similar sizes. For hole-doped compounds, the hole pockets at Γ enlarge while the electron

pockets shrink. For heavily electron-doped compounds such as the electron-doped chalcogenides, the hole pockets disappear while large electron pockets remain at M.

One of the fundamental questions after the discovery of the FeSCs was whether it is appropriate to model them as localized systems or itinerant systems. On one hand, the observed large spectral weight in the fluctuating magnetic spectrum⁵ tends to suggest the former, while the high density of states found near E_F compared to the cuprates⁶ seems to suggest the latter. As we know now, neither picture is fully complete. We will show in the following that there is a large systematic spread of electron correlation strength among different FeSCs, and more importantly, this occurs in a strongly orbital-dependent way.

This trend can be qualitatively seen by comparing representative compounds from the iron phosphides to the iron arsenides and to the iron chalcogenides (Fig. 2). Electron correlation renormalizes the electronic bandwidth. From ARPES data, one way to quantify the strength of correlation is to extract the ratio of the non-interacting bandwidth calculated from local density approximation (LDA) and experimentally measured bandwidth, which is the renormalization factor⁷. Fig. 2a-c shows the band dispersions along the high symmetry direction Γ -M observed in the paramagnetic state of a phosphide (SrFe_2P_2), an arsenide (NaFeAs), and a chalcogenide ($\text{FeSe}_{0.44}\text{Te}_{0.56}$), plotted in the same energy window, where the d_{yz} band is marked in green and d_{xy} blue. There are two observations to make: i) the bandwidth of all bands systematically narrows from phosphide to the arsenide to the chalcogenide, which is also seen in the increase of

the renormalization factors, and ii) the bandwidth of d_{xy} narrows at a much faster rate than that of d_{yz} from the phosphides to the chalcogenides. These two observations suggest that both the overall electron correlation strength and orbital-selectivity, which is defined here as the ratio in the band renormalization between the d_{xy} band and d_{yz} band, increase from the iron phosphides to the iron chalcogenides. In the following section, we systematically demonstrate these trends and discuss factors that correlate with these two parameters.

Considering the three active orbitals near E_F , the d_{xz} and d_{yz} orbitals are bound by C_4 symmetry to be degenerate in the tetragonal state. The d_{xy} orbital, however, does not necessarily need to behave in the same way as d_{xz}/d_{yz} . Hence we examine each orbital in turn. For the bands near E_F , the d_{yz} band is the band that can be observed most completely under common polarization setups, with its band top at Γ and band bottom between Γ and M (Fig. 1d). Here we extract its bandwidth from ARPES literature and compare with available LDA calculations (Table 1).

Figure 2d shows the d_{yz} renormalization factors for FeSC compounds measured in the normal state as a function of the Fe-Pn/Ch bond length. To avoid complications from doping effects, we only plot undoped parent compounds here where the electron filling, n , is 6. First of all, we see a clear trend with a continuous spread of renormalization factors from the phosphides at the bottom to the 122 arsenides to the 111 arsenides and to the chalcogenides. The d_{yz} renormalization factor, which is a measure of overall correlation strength, increases with the Fe-Pn/Ch bond length. Intuitively, longer bond length reduces electron hopping and therefore the kinetic energy, hence leading to more localized behavior. However, similar plot for the d_{yz} and

d_{xy} renormalizations as a function of the lattice a (effectively Fe-Fe bond length) does not show as clear a trend over all compounds (Fig. 3a,c). As d_{yz} is extended in the out-of-plane direction and d_{xy} is mostly in plane, the lack of clear trend in both renormalizations against lattice a suggests that electron hopping is dominated by the indirect path of Fe-Pn/Ch-Fe rather than that of direct Fe-Fe bond. The d_{yz} renormalization factor also has strong correlation with related structural parameters such as anion height and bond angle, which both directly relate to the Fe-Pn/Ch bond length⁸. Similar dependence of correlation strength on structural parameters is also seen in optical data within the BaFe_2As_2 family⁹ and photoemission data within the heavily electron-doped iron chalcogenides¹⁰. For other structural parameters such as the lattice constant c , the correlation with bandwidth renormalization is not obvious across families (Fig. 3b,d).

Structural parameters are not the only factors that correlate with the overall correlation strength. A second factor is electron filling⁷. In Fig. 2e we plot the d_{yz} bandwidth renormalization versus the electron filling for doped compounds of two series, the BaFe_2As_2 series and the LiFeAs series. To put this plot in perspective, we also overlay the electron (Co) and hole (K) doped phase diagram of BaFe_2As_2 on the horizontal axis. The data points for this series range from those taken from KFe_2As_2 ($n = 5.5$) to BaNi_2As_2 ($n = 8$). Here we note that the undoped parent compounds of FeSC has $n = 6$, which is not half-filling as the case of the parent compounds of the cuprates. True half-filling for the Fe 3d orbitals is $n = 5$. This explains the asymmetry of the overall correlation with respect to the undoped parent compounds of FeSC^{7,9}. The electron correlation is weak far away from $n = 5$ for the heavily electron-doped compounds, and diverges

towards $n = 5$ on the hole-doped side. However, it is interesting to note that, under this scenario, the known undoped iron pnictides are effectively on the electron-doped side of the true half filling. In analogy to the cuprates, there may be an equivalent regime of superconductivity on the hole-doped side, as has been recently theoretically suggested¹¹⁻¹².

In Fig. 2f we plot all the compounds (including those with different electron fillings) with sufficient information from literature on a 2D plot with electron filling and the Fe-Pn/Ch bond length, and use color to indicate the strength of d_{yz} bandwidth renormalization factor. Here we see as demonstrated before, both reducing electron filling towards $n = 5$ and lengthening the Fe-Pn/Ch bond length increase overall correlation.

Next, we discuss factors that affect the orbital-selectivity. Since the d_{xy} orbital is the most correlated of the orbitals, quantitatively, we extract the ratio of the renormalization factors of the d_{xy} band and the d_{yz} band. In Fig. 2h we plot this for all compounds we found from literature against the Pn/Ch-Fe-Pn/Ch bond angle. A clear trend is seen where smaller bond angle, as in the case of the chalcogenides, leads to strong selectivity; whereas bigger bond angle, as in the case of the phosphides, leads to almost no selectivity. This is because smaller bond angle results in a vertically elongated tetragon, which reduces hopping more dramatically for the in-plane d_{xy} orbital than d_{xz}/d_{yz} orbitals, considering hopping is dominantly mediated through the Pn/Ch, which reside out of the Fe plane. Besides the bond angle, Fig. 2g also shows another factor that correlates with orbital-selective correlation—the overall electron correlation represented by the

d_{yz} renormalization factor. It demonstrates that among all FeSCs, the stronger the overall correlation, the stronger the orbital-selectivity in the d_{xy} orbital. This has been discussed in previous theoretical work as due to the tendency towards a Hund's metal phase, where Hund's coupling increases orbital differentiation and independence by suppressing inter-orbital correlations^{8,13-14}. In Fig. 2i, we plot the orbital-selectivity as a function of both bond angle and overall correlation strength for all compounds. We see that these dependences are not only true within a family of FeSC, but systematically spread among all FeSC compounds.

As orbital-selectivity increases, an interesting phenomenon occurs in the strongly correlated members of FeSCs—a tendency towards an orbital-selective Mott phase (OSMP). In Fig. 4a, we plot the bond length dependence of the renormalization factors of the d_{xy} orbital for undoped FeSCs ($n = 6$), which is the most correlated orbital. Comparing to the equivalent plot for d_{yz} (Fig. 2d), we see that the dynamic range of the d_{xy} orbital is five-fold of that of d_{yz} . This again showcases the strong orbital differentiation among the FeSCs towards the strongly correlated members. When this differentiation is strong, as in the iron chalcogenides, the normal state of these materials is sufficiently close to an OSMP such that raising temperature has been observed to push them into the OSMP where the d_{xy} orbital completely loses its spectral weight while other orbitals remain itinerant (Fig. 4b)¹⁵. This has in fact been observed universally for different iron chalcogenides including Fe(Te,Se), KFe_2Se_2 , and monolayer FeSe film grown on SrTiO_3 ¹⁶⁻¹⁹ and Nb:BaTiO₃/KTaO₃ heterostructures²⁰. Even for the most correlated iron arsenide, KFe_2As_2 , evidence for decoherence of the d_{xy} orbital has been observed by transport measurements²¹. Here

we see that the tendency towards the OSMP in the chalcogenides is not accidental, but grows naturally from an increasingly selective orbital correlation systematically in all FeSCs.

Both the spread of electron correlation strength and the increasing orbital selectivity are perhaps what makes it difficult to develop a unified theoretical model for all FeSCs. On one side of the spectrum the orbitals are mostly itinerant with almost no orbital selectivity while on the other side strong orbital decoupling due to Hund's coupling results in one of the orbitals approaching localization. Nonetheless, this orbital-selectivity is a behavior unique and essential to the multi-orbital physics of the FeSCs in contrast to the single-band physics of the cuprates. Its importance is especially evident for the compounds on the strongly correlated side such as the chalcogenides. These behaviors have led to interesting theoretical proposals where one redefines the phase diagram using an average orbital filling, showing a gradual approach from superconductivity towards a Mott insulating state via an OSMP¹³, while another proposes that in the strongly orbital-selective regime, the d_{xy} orbital is near half-filling¹⁴. Both suggest parallels reminiscent of the cuprate problem.

The nematic state

In a typical phase diagram of iron-based superconductors, the material in the underdoped regime goes through two transitions and enters the nematic state and the SDW state at low temperatures²⁻³. The multi-orbital nature not only leads to orbital-dependent band renormalization in the normal state, but also plays an important role in driving the system into

these symmetry-breaking states. The nematic phase is marked by a tetragonal to orthorhombic structural transition at T_S , where C_4 rotational symmetry is broken down to C_2 symmetry without breaking the translational symmetry. With the orthorhombic distortion, material forms natural twin domains. Hence for macroscopic probe like ARPES where the beam spot is larger than the typical domain size (Fig. 5a), the photoemission signal becomes the superposition of band structures from two orthogonal domains. As a result, complex band reconstructions were reported in early ARPES studies²²⁻²⁴. Subsequently, it was realized that samples with a single domain could be achieved by applying a uniaxial pressure mechanically on the sample²⁵⁻²⁶. The intrinsic band structure of the C_2 state was then revealed by ARPES measurements on detwinned crystals of $BaFe_2As_2$ ²⁷⁻²⁹, $NaFeAs$ ³⁰⁻³¹, $FeSe$ ³²⁻³⁵, and $FeSe$ films³⁶⁻³⁷. Figure 5b shows an example of detwinned $NaFeAs$ measured in the nematic state, where the d_{yz} band (green) along the slightly longer axis is shifted up while the d_{xz} band (red) along the shorter axis is shifted down. In the tetragonal state above T_S , these two bands are degenerate in energy. This shift in opposite directions in the orthorhombic state indicates the breaking of the C_4 symmetry in the orbital degree of freedom. This generic upward shift of d_{yz} orbital and downward shift of d_{xz} orbital is observed in all measurements of detwinned FeSCs in the nematic phase²⁷⁻³⁷. Importantly, the relatively large energy scale of this orbital splitting cannot be a trivial consequence of the less than 1% orthorhombicity²⁷. Hence the orbital anisotropy is unlikely to be a simple result of the lattice, but rather suggests the manifestation of electronic nematicity, consistent with the original discovery of large resistivity anisotropy in this phase²⁵. We note that, on top of the discussed band separation, an additional small band splitting has been observed by

ARPES in FeSe³⁸⁻³⁹, which induced hot debates on how to extract the correct nematic energy splitting from the ARPES data. The energy scale of the large band separation scales with the nematic transition temperature in all measured FeSCs and thus likely represents the strength of nematic order. Moreover, very recent data on detwinned FeSe clearly shows the two bands with large energy separation to belong to orthogonal directions⁴⁰, hence consistent with the previous understanding that the d_{xz} and d_{yz} orbitals are indeed split by ~ 50 meV in the nematic phase, similar to the pnictides.

The discovery of energy splitting of d_{xz} and d_{yz} bands has been viewed as an evidence for the existence of orbital order in the nematic state. It has been proposed that the on-site occupation difference between d_{xz} and d_{yz} orbitals triggers a ferro-orbital ordering, which consequently drives the system into the nematic state⁴¹⁻⁴³. In most band calculations where only the on-site occupation difference is considered, the ferro-orbital order results in an energy splitting of d_{xz} and d_{yz} bands that is almost constant throughout the BZ. Experimentally, clear delineation of the momentum dependence of the d_{xz} and d_{yz} splitting has not been carefully examined for most FeSCs, because the close proximity of the magnetic and structural transitions prevents a clear separation of the effects of the two phases. FeSe, which does not have a magnetic transition⁴⁴, offers a clean case for examining the nature of nematic order and associated nematic transition in detail. Figure 5c shows the band dispersions along the high symmetry direction Γ -M of a twinned multi-layer FeSe film grown on SrTiO₃³⁶, which resembles bulk FeSe crystal. On a twinned sample, the longer and shorter orthogonal high symmetry directions from orthogonal

domains are superpositioned along the same cut. Hence the shifted d_{xz}/d_{yz} bands appear as effectively split in energy below T_S . From this data, two important observations can be made. Firstly, the d_{xz}/d_{yz} bands, which are degenerate above T_S , are split in the same fashion as in other FeSCs. Secondly, a clear momentum-dependence is seen in this orbital anisotropy. As shown in Fig. 5d, instead of being constant, a finite energy splitting at Γ first decreases to zero and then increases again, reaching its maximum at the M point. The momentum-dependence of the energy splitting is consistent with $BaFe_2As_2$ and $NaFeAs$, where the orbital anisotropy is small at Γ but large at M²⁷. Furthermore, the momentum dependence of orbital anisotropy is non-monotonic, which may be understood by considering a band splitting ($E_{yz}-E_{xz}$) that switches sign between Γ and M (Fig. 5e). This has indeed been experimentally observed in detwinned FeSe bulk crystal^{35,40}. This non-trivial momentum dependence of the d_{xz}/d_{yz} energy splitting suggests that the simple on-site occupation difference between d_{xz}/d_{yz} orbitals is unlikely to be the driving force of the nematic phase. Instead, other mechanisms such as anisotropic hopping of the d_{xz}/d_{yz} orbitals⁴⁵⁻⁴⁶, Pomeranchuk instability⁴⁷, orbital-dependent correlation effect⁴⁸, and orbital-selective spin fluctuations⁴⁹ could all result in different renormalization and/or shift of the d_{xz}/d_{yz} bands in the nematic state.

While the d_{xz}/d_{yz} orbital anisotropy has attracted great attentions, the d_{xy} orbital has not been considered in most theoretical models, partly due to the lack of experimental evidence for a clear participation of d_{xy} orbital in the electronic reconstructions and the assumption that it does not contribute to C_4 symmetry breaking. However, as illustrated in Figs. 5f and 5g, to fully explain

the three electron bands observed in the nematic phase at the M point on this twinned sample, the shift of the d_{yz} and d_{xz} bands in opposite directions is insufficient, in addition, the d_{xy} band along the longer x-direction must shift down in energy while the counterpart d_{xy} band along the shorter y-direction must remain unshifted³⁶. Furthermore, the magnitude of the energy splitting of the d_{xy} band along two perpendicular directions is comparable to the energy splitting of the d_{xz}/d_{yz} orbitals, which further suggests the complexity of the orbital anisotropy in the nematic state.

The observed band reconstruction and its orbital dependence put strong constraints on theoretical models regarding the nematic state. On one hand, while most theories consider only the d_{xz}/d_{yz} orbitals, the ARPES results suggest that all three orbitals play an important role in driving the nematic state. As one theoretical study shows, the coupling of the d_{xy} orbital to the nematic order parameter is necessary for predicting the correct gap symmetry in FeSe⁵⁰. On the other hand, the energy scale of the band reconstruction shows a strong momentum dependence, indicating that the anisotropy is unlikely to be dominated by the on-site occupation difference between the d_{xz} and d_{yz} orbitals. Instead, other mechanisms must be considered to correctly describe the momentum-dependence orbital anisotropy.

The spin-density wave order

Next, we discuss the role of different orbitals in forming the collinear SDW order. The SDW order has been found to couple strongly with the nematic order in most cases. On top of the

rotational symmetry breaking, the SDW order further breaks the translational symmetry. As a result, the BZ reduces and bands fold across the SDW zone boundary. Spectrally, the signatures of the SDW band reconstruction are very distinct from that of the nematic phase. Instead of the band shift, SDW gaps open where folded bands cross original bands. It is simpler to illustrate the details of the band folding by unfolding the bands into the 1-Fe BZ, where the folding occurs strictly along the AFM direction Γ - M_x but not along the FM direction (Fig. 6a). Here, the Γ point has two hole pockets from the d_{xz} and d_{yz} hole bands. At the M_x point, an electron pocket appears that is of d_{xy} character along the AFM direction and d_{yz} along the FM direction. At the M_y point, another electron pocket appears with d_{xy} along the FM direction and d_{xz} along the AFM direction. At the Γ' point, in some of the iron-arsenide compounds, lives the third hole pocket of d_{xy} character. With SDW folding, the Γ and M_x points fold unto each other, while the M_y and Γ' points fold unto each other.

Next, we discuss the detailed band reconstruction around these two folded points using data from detwinned BaFe_2As_2 , which can be revealed by using different polarizations. For the folded Γ - M_x cut (Fig. 6b), along the AFM direction, the d_{xy} electron band from M_x folds unto the d_{xz} and d_{yz} hole bands around Γ , but little or no SDW gap appears along this high symmetry direction where folded bands cross. Along the orthogonal FM direction at this same point (Fig. 6c), the d_{yz} electron band crosses the d_{xz}/d_{yz} bands, forming an SDW gap on the order of $\sim 30\text{meV}$ between the d_{yz} bands, which can be seen in both the d_{yz} hole band and the d_{yz} electron band. For the folded M_y - Γ' point (Fig. 6d), along the AFM direction, the d_{xz} electron band

crosses the d_{xy} hole band, opening an SDW gap that saddles E_F , with a gap size bigger than 50meV. Along the orthogonal FM direction at this point (Fig. 6e), the d_{xy} hole and electron bands cross each other, opening an SDW gap that is larger than 50meV. Overall, we see that the SDW gap opens at the folded band crossings in an orbital-dependent way. The biggest SDW gaps occur in the d_{xy} bands around the $M_y-\Gamma'$ point. The SDW gap is moderate for the d_{yz} bands at the $\Gamma-M_x$. For the d_{xz} hole bands, the SDW gap is the smallest, resulting in dominant d_{xz} orbital weight near the Fermi energy in the SDW state⁵¹. Four SDW gap nodes exist along the high symmetric directions due to the incompatible symmetries of the crossing bands⁵². As a result, the Fermi surface reconstructs drastically, forming four small Fermi pockets along both the $\Gamma-M_x$ and $\Gamma-M_y$ directions (lower panel of Fig. 6a).

The SDW order has been described in both weak- and strong- coupling theories. It is still largely debated whether the SDW is originated from the super-exchange interaction of local moments or the Fermi surface nesting of itinerant electrons^{5,53-58}. The orbital-dependence of the band reconstruction in the SDW state suggests an orbital-selective magnetism in the iron-based superconductors. It has been proposed that the magnetic moments originate mainly from the d_{xy} and d_{yz} orbitals instead of the d_{xz} orbital in the SDW state⁵⁹⁻⁶¹, which is consistent with the orbital-dependent SDW gaps observed here. The multi-orbital nature of the SDW state also explains the dual character of the magnetic moments observed by neutron scattering experiment⁵³. Both the local property of d_{xy} orbital and the itinerancy of the d_{yz}/d_{xz} orbitals should be considered in constructing the microscopic model of the SDW state in iron-based

superconductors.

The superconducting state

Finally, we discuss the role of orbitals in the superconducting state. While the superconducting gap in cuprates can be fitted by a simple $d_{x^2-y^2}$ gap function across all different families, the gap symmetry in FeSCs has a complex distribution in momentum space that varies among different families⁶²: while largely isotropic gaps have been observed in $Ba_{1-x}K_xFe_2As_2$ ⁶² consistent with s_{\pm} symmetry, strong gap anisotropy or even gap nodes have been reported in $BaFe_2(As_{1-x}P_x)_2$ ⁶³⁻⁶⁴, $LiFeP$ ⁶⁵, bulk $FeSe$ ⁶⁶, $FeSe_{1-x}S_x$ ⁶⁷, and $FeSe$ films⁶⁸. In cases like 1ML $FeSe$ thin film, the gap function cannot be fitted by single trigonometric gap functions under s_{\pm} , d-wave, or extended s-wave gap symmetries⁶⁹. This contrasting behavior is intimately connected to the multi-band multi-orbital nature of the underlying electronic structure and again implies the non-trivial role which orbital physics plays in the FeSCs.

First of all, the Fermi surface of FeSCs consists of multiple Fermi pockets with distinctive orbital characters. Such Fermi surface topology allows Cooper pairs to scatter via intra- or inter-orbital scattering channels. One critical question is which scattering channel is more important for superconducting pairing. The intra-orbital pairing would result in an orbital dependent superconducting gap while the inter-orbital pairing tends to generate equivalent gaps among different orbitals. Experimentally, multi-gap behavior has been observed in several iron-based compounds by scanning tunneling microscopy (STM)⁷⁰⁻⁷¹ and transport

measurements⁷²⁻⁷³. ARPES studies on $\text{Ba}_{1-x}\text{K}_x\text{Fe}_2\text{As}_2$ and LiFeAs show that the superconducting gap on the d_{xz}/d_{yz} hole pockets is much larger than that on the d_{xy} hole pocket⁶². All these results seem to suggest the dominating role of intra-orbital pairing in FeSCs.

Another important question often asked is which orbital plays the most important role for superconductivity. This, too, seems to vary between different compounds. For most iron-pnictide compounds studied with comparable hole and electron pockets, the d_{xz}/d_{yz} hole pockets show larger superconducting gap than the d_{xy} hole pocket^{62,74}, suggesting the importance of d_{xz}/d_{yz} orbitals to superconductivity. Consistently, in $\text{LiFe}_{1-x}\text{Co}_x\text{As}$ and $\text{Ba}(\text{Fe}_{1-x}\text{Co}_x)_2\text{As}_2$, when the d_{xz}/d_{yz} hole pockets vanish with electron doping, superconductivity is strongly suppressed⁷⁵⁻⁷⁶. On the contrary, for heavily electron-doped iron-selenide superconductors with only electron pockets, the superconducting gap of 1ML FeSe film show maxima on the d_{xy} electron bands⁷⁷. Furthermore, in bulk FeSe crystal, where the sample is continuously surface-doped to enhance superconductivity, it is reported that the appearance of the d_{xy} electron pocket on the Fermi surface at the M point coincides with the beginning of the second superconducting dome with higher T_C and different pairing symmetry⁷⁷. Interestingly, another work on the pnictide compound $\text{Ca}_{10}(\text{Pt}_4\text{As}_8)(\text{Fe}_{2-x}\text{Pt}_x\text{As}_2)_5$ shows relatively high T_C with the presence of only the d_{xy} hole pocket at Γ ⁷⁸. This may on one hand suggest the importance of the d_{xy} orbital to superconductivity, on the other hand highlight the strong correlation between inter-pocket (intra-orbital) scattering and superconductivity.

The level of material-dependence reported in the past decade has been somewhat puzzling and perhaps disappointing for the ultimate goal of finding a simple unifying description of superconductivity. However, this may be well expected when we consider the multi-orbital nature of the FeSCs. As this is a new dimension which has been lacking from the machinery developed out of the cuprate problem, theoretical work taking into account the orbital degree of freedom has been very limited, but several work have already showed promise. From the strong coupling approach using a multiorbital t - J_1 - J_2 model, one study showed that the orbital-selectivity results in a gap anisotropy that is also orbital-dependent⁷⁹. From a weak-coupling approach, a very recent theoretical study based on spin fluctuations taking into consideration the orbital-selective renormalization that modulates the coherent spectral weight of different orbitals was able to reproduce the observed momentum-dependent gap structure of monolayer FeSe and LiFeAs⁸⁰. Other theoretical works have also proposed interesting mechanisms by which the FeSCs and cuprates could be united⁸¹⁻⁸². These work importantly demonstrate that behind the apparent gap variations amongst FeSCs there may be a common underlying pairing mechanism, and the source of the material-dependence may be the different degree of orbital-selective correlation effects, which tune the dominant orbitals that are manifested.

Discussion

We first summarize the key findings of the four major phases discussed:

- The normal state:
 - Electron correlations systematically and continuously spread across FeSC families tuned by two factors: i) the Fe-Pn/Ch bond length, and ii) electron doping away from true half-filling at $n=5$.
 - Electron correlations are orbital-dependent, with the d_{xy} orbital being the most localized. The strength of orbital-selectivity is tuned by i) overall correlation strength, and ii) bond angle, eventually reaching an orbital-selective Mott phase where the d_{xy} orbital is completely localized while other orbitals remain itinerant.
- The nematic state:
 - There is significant C_4 symmetry breaking in the orbital degree of freedom at the onset of the structural transition beyond the effect of the lattice distortion. In particular, the d_{yz} -dominant band is observed to shift up while the d_{xz} -dominated band is observed to shift down, albeit in a strongly-momentum dependent way.
 - The d_{xy} orbital is also observed to participate by exhibiting a splitting in energy that is comparable to that of d_{xz}/d_{yz} orbitals, suggesting an anisotropic hopping origin rather than ferro-orbital order.
- The spin density wave order:
 - Band folding occurs, producing SDW gaps that are the largest in the d_{xy} orbital, moderate in the d_{yz} orbital, and smallest in the d_{xz} orbital.
- The superconducting state:
 - Superconducting gaps are generally observed to be multi-gap, suggesting

dominance of intra-orbital pairing.

- Gap functions cannot be described by single trigonometric gap functions, and also vary among families, suggesting the complex role of intra-orbital pairing and multi-orbital FS.

Having discussed the normal state, the nematic state, the magnetic state, and the superconducting state separately, we now discuss the relationship between these phases. From the normal state properties, we see that there is a systematic spread of electronic correlation over all the FeSCs, with a large dependence on certain structural parameters such as the bond length and bond angle. As has been shown, the superconducting temperature, T_C , is also highly dependent on the bond angle⁸³. Hence superconductivity is expected to be optimized at intermediate electron correlation strength. The nematic phase and the collinear SDW phase are often discussed together. Here we see that the two orders can be strongly coupled, as in most iron arsenides, but not necessarily always the case, as in FeSe. Regardless of the strength of coupling of these two orders, we see that the spectral signature and magnitude for the nematic order is the same across different materials. The nature of these two phases to superconductivity is competitive. As has been reported, the spectral order parameters of these two orders both decrease at the onset of superconductivity⁸⁴, similar to the macroscopic order parameters of the lattice orthorhombicity and the magnetic moment⁸⁵.

For all three phases discussed, we also see a strong orbital-dependence. Hund's coupling

suppresses orbital interaction, separating the d_{xy} orbital from the largely degenerate d_{xz}/d_{yz} . This coupled with crystal field splitting effectively makes the d_{xy} orbital the most strongly correlated, as seen in the normal state, and in some cases close to half-filling while the overall filling is effectively on the electron-doped side. This occurrence enables some behaviors of the d_{xy} orbital in the FeSCs to become relevant to the cuprates, such as the observation of OSMP in the most correlated iron chalcogenides. We have also seen that the d_{xy} orbital actively participates in the nematic and magnetic competing phases to superconductivity, by both developing a non-trivial anisotropy below T_S and the largest SDW gap below T_{SDW} . The d_{xz}/d_{yz} orbitals, on the other hand, are less correlated than d_{xy} and maintains a certain level of itinerancy due to their degeneracy and effective electron-doping away from half-filling. This degeneracy also gives them a more active role in the nematic phase, where the degeneracy is lifted below T_S .

Overall, we see that the orbital-dependence in the FeSC plays a nontrivial role. The systematic spread of orbital-selective electron correlations across different FeSC families may well be the origin of material-dependent variations that is manifested when the participation of different orbitals is enhanced or suppressed in different phases. When taken under this perspective, there is still hope that the underlying mechanism for superconductivity and competing phases in the FeSCs and perhaps even the cuprates may take on a unified simple form, upon which the orbital-selective physics adds on an essential and colorful light.

Acknowledgements

The authors would like to thank Véronique Brouet, Thomas Devereaux, Rafael Fernandes, and Leni Bascones for enlightening discussions, and David Singh for kindly providing LDA calculations for SrFe_2P_2 . This work was supported by the U.S. Department of Energy, Office of Science, Basic Energy Sciences, Materials Sciences and Engineering Division under contract DE-AC02-76SF00515. Stanford Synchrotron Radiation Lightsource and the Advanced Light Source are both operated by the U.S. Department of Energy, Office of Science, Office of Basic Energy Sciences.

Competing Interests

The authors declare no competing financial interests.

Author Contributions

M.Y. organized the section on the normal state. Y. Z. organized the sections on the nematic, spin-density-wave, and superconducting states. Z.X.S. and D.H.L. advised and oversaw the overall structure of the manuscript. All authors contributed to the writing of the manuscript.

Data availability

The data sets used for the normal state properties were taken from available literature and the references are all provided in Table 1.

References

1. Kamihara, Y. *et al.* Iron-based layered superconductor $\text{LaO}_{1-x}\text{F}_x\text{FeAs}$ ($x=0.05-0.12$) with $T_C = 26\text{K}$. *J. Am. Chem. Soc.* **130**, 3296-3297 (2008).
2. Paglione, P. *et al.* High-temperature superconductivity in iron-based materials. *Nat. Phys.* **6**, 645-658 (2010).
3. Johnston, D. The puzzle of high temperature superconductivity in layered iron pnictides and chalcogenides. *Adv. Phys.* **59**, 803-1061 (2010).
4. Bascones, E., Valenzuela, B., and Calderón, M. J. Magnetic interactions in iron superconductors: A review. *C. R. Physique* **17**, 36–59 (2016).
5. Dai, P. *et al.* Magnetism and its microscopic origin in iron-based high-temperature superconductors. *Nat. Phys.* **8**, 709-718 (2012).
6. Lu, D.-H. *et al.* Electronic structure of the iron-based superconductor LaOFeP . *Nature* **455**, 81-84 (2008).
7. Ye, Z. *et al.* Extraordinary Doping Effects on Quasiparticle Scattering and Bandwidth in Iron-Based Superconductors. *Phys. Rev. X* **4**, 031041 (2014).
8. Yin, Z. *et al.* Kinetic frustration and the nature of the magnetic and paramagnetic states in iron pnictides and iron chalcogenides. *Nat. Mat.* **10**, 932-935 (2010).
9. Nakajima, M. *et al.* Normal-state charge dynamics in doped BaFe_2As_2 : Roles of doping and necessary ingredients for superconductivity. *Sci. Rep.* **4**, 5873 (2014).

10. Niu, X. H. *et al.* A unifying phase diagram with correlation-driven superconductor-to-insulator transition for the 122 series of iron chalcogenides. *Phys. Rev. B* **93**, 054516 (2016).
11. Pizarro, J. M. *et al.* Strong correlations and the search for high-T_c superconductivity in chromium pnictides and chalcogenides. *Phys. Rev. B* **95**, 075115 (2017).
12. Edelmann, M., Sangiovanni, G., Capone, M., and de' Medici, L. Chromium analogs of Iron-based superconductors. *Phys. Rev. B* **95**, 205118 (2017).
13. de Medici, L. *et al.* Selective Mott Physics as a Key to Iron Superconductors. *Phys. Rev. Lett.* **112**, 177001 (2014).
14. Yu, R. and Si, Q. Orbital-Selective Mott Phase in Multiorbital Models for Alkaline Iron Selenides K_{1-x}Fe_{2-y}Se₂. *Phys. Rev. Lett.* **110**, 146402 (2013).
15. Yi, M. *et al.* Observation of Temperature-induced Crossover to an Orbital-Selective Mott Phase in A_xFe_{2-y}Se₂ (A=K, Rb) Superconductors. *Phys. Rev. Lett.* **110**, 067003 (2013).
16. Yi, M. *et al.* Observation of universal strong orbital-dependent correlation effects in iron chalcogenides. *Nat. Comm.* **6**, 7777 (2015).
17. Wang, Z. *et al.* Orbital-selective metal-insulator transition and gap formation above T_C in superconducting Rb_{1-x}Fe_{2-y}Se₂. *Nat. Comm.* **5**, 3202 (2014).
18. Ding, X. *et al.* Strong and nonmonotonic temperature dependence of Hall coefficient in superconducting K_xFe_{2-y}Se₂ single crystals. *Phys. Rev. B* **89**, 224515 (2014).

19. W, Li. *et al.* Mott behaviour in $K_xFe_{2-y}Se_2$ superconductors studied by pump-probe spectroscopy. *Phys. Rev. B* **89**, 134515 (2014).
20. Pu, Y. J. *et al.* Temperature-induced orbital selective localization and coherent-incoherent crossover in single-layer FeSe/Nb:BaTiO₃/KTaO₃. *Phys. Rev. B* **94**, 115146 (2016).
21. Hardy, F. *et al.* Evidence of strong correlations and coherence-incoherence crossover in the iron pnictide superconductor KFe₂As₂. *Phys. Rev. Lett.* **111**, 027002 (2013).
22. Yi, M. *et al.* Electronic structure of the BaFe₂As₂ family of iron-pnictide superconductors. *Phys. Rev. B* **80**, 024515 (2009).
23. Hsieh, D. *et al.* Experimental determination of the microscopic origin of magnetism in parent iron pnictides. arXiv: 0812.2289 (2008).
24. Yang, L. X. *et al.* Electronic structure and unusual exchange splitting in the spin-density-wave state of the BaFe₂As₂ parent compound of iron-based superconductors. *Phys. Rev. Lett.* **102**, 107002 (2009).
25. Chu, J.-H. *et al.* In-Plane Resistivity Anisotropy in an Underdoped Iron Arsenide Superconductor. *Science* **329**, 824-826 (2010).
26. Tanatar, M. A. *et al.* Uniaxial-strain mechanical detwinning of CaFe₂As₂ and BaFe₂As₂ crystals: Optical and transport study. *Phys. Rev. B* **81**, 184508 (2010).
27. Yi, M. *et al.* Symmetry-breaking orbital anisotropy observed for detwinned Ba(Fe_{1-x}Co_x)₂As₂ above the spin density wave transition. *Proc. Natl. Acad. Sci.* **108**, 6878-6883 (2011).

28. Kim, Y. *et al.* Electronic structure of detwinned BaFe₂As₂ from photoemission and first principles. *Phys. Rev. B* **83**, 064509 (2011).
29. Sonobe, T. *et al.* Orbital anisotropy underlying the superconducting dome in BaFe₂(As_{1-x}P_x)₂ superconductors. arXiv:1512.02389 (2015).
30. Yi, M. *et al.* Electronic reconstruction through the structural magnetic transitions in detwinned NaFeAs. *New J. Phys.* **14**, 073019 (2012).
31. Zhang, Y. *et al.* Symmetry breaking via orbital-dependent reconstruction of electronic structure in uniaxially strained NaFeAs. *Phys. Rev. B* **85**, 085121 (2012).
32. Nakayama, K. *et al.* Reconstruction of Band Structure Induced by Electronic Nematicity in FeSe Superconductor. *Phys. Rev. Lett.* **113**, 237001 (2014).
33. Shimojima, T. *et al.* Lifting of xz/yz orbital degeneracy at the structural transition in detwinned FeSe. *Phys. Rev. B* **90**, 121111 (2014).
34. Watson, M. *et al.* Emergence of the nematic electronic state in FeSe. *Phys. Rev. B* **91**, 155106 (2015).
35. Suzuki, Y. *et al.* Momentum-dependent sign-inversion of orbital polarization in superconducting FeSe. *Phys. Rev. B* **92**, 205117 (2015).
36. Zhang, Y. *et al.* Distinctive orbital anisotropy observed in the nematic state of FeSe thin film. *Phys. Rev. B* **94**, 115153 (2016).
37. Tan, S. *et al.* Interface-induced superconductivity and strain-dependent spin density waves in FeSe/SrTiO₃ thin films. *Nat. Mat.* **12**, 634-640 (2013).

38. Fedorov, A. *et al.* Effect of nematic ordering on electronic structure of FeSe. *Sci. Rep.* **6**, 36834 (2016).
39. Watson, M. D. *et al.* Evidence for unidirectional nematic bond ordering in FeSe. *Phys. Rev. B* **94**, 201107(R) (2016).
40. Watson, M. D., *et al.* Haghhighirad, A. A., Rhodes, L. C., Hoesch, M., and Kim, T. K. Electronic anisotropies in the nematic phase of FeSe. arXiv: 1705.02286.
41. Lv, W. *et al.* Orbital ordering and unfrustrated $(\pi,0)$ magnetism from degenerate double exchange in the iron pnictides. *Phys. Rev. B* **80**, 224506 (2009).
42. Chen, C. C. *et al.* Orbital order and spontaneous orthorhombicity in iron pnictides. *Phys. Rev. B* **82**, 100504(R) (2010).
43. Lee, C.-C. *et al.* Ferro-Orbital Order and Strong Magnetic Anisotropy in the Parent Compounds of Iron-Pnictide Superconductors. *Phys. Rev. Lett.* **103**, 267001 (2009).
44. Medvedev, S. *et al.* Electronic and magnetic phase diagram of beta-Fe(1.01)Se with superconductivity at 36.7 K under pressure. *Nat. Mat.* **8**, 630-633 (2009).
45. Su, Y., Liao, H., and Li, T. The form and the origin of the orbital ordering in the electronic nematic phase of the Iron-based superconductors. *J. Phys.: Condens. Matter* **27**, 105702 (2015).
46. Li, T. and Su, Y. Driving force of the orbital-relevant electronic nematicity in Fe-based superconductors. arXiv: 1703.09841.
47. Chubukov, A., Khodas, M., and Fernandes, R. M. Magnetism, Superconductivity, and

Spontaneous Orbital Order in Iron-Based Superconductors: Which Comes First and Why?

Phys. Rev. X **6**, 041045 (2016).

48. Fanfarillo, L., Giovannetti, G., Capone, M. and Bascones, E. Nematicity at the Hund's metal crossover in iron superconductors. *Phys. Rev. B* **95**, 144511 (2017).
49. Fanfarillo, L. *et al.* Orbital-dependent Fermi surface shrinking as a fingerprint of nematicity in FeSe. *Phys. Rev. B* **94**, 155138 (2016).
50. Kang, J. and Fernandes, R. M. Superconductivity in FeSe Thin Films Driven by the Interplay between Nematic Fluctuations and Spin-Orbit Coupling. *Phys. Rev. Lett.* **117**, 217003 (2016).
51. Shimojima, T. *et al.* Orbital-Dependent Modifications of Electronic Structure across the Magnetostructural Transition in BaFe₂As₂. *Phys. Rev. Lett.* **104**, 057002 (2010).
52. Ran, Y., Wang, F., Zhai, H., Vishwanath, A., and Lee, D.-H. *Phys. Rev. B* **79**, 014505 (2009).
53. Dai, P. *et al.* Antiferromagnetic order and spin dynamics in iron-based superconductors. *Rev. Mod. Phys.* **87**, 855-896 (2015).
54. Fang, C. *et al.* Theory of electron nematic order in LaFeAsO. *Phys. Rev. B* **77**, 224509 (2008).
55. Mazin, I. I. *et al.* Unconventional Superconductivity with a Sign Reversal in the Order Parameter of LaFeAsO_{1-x}F_x. *Phys. Rev. Lett.* **101**, 057003 (2008).
56. Kuroki, K. *et al.* Unconventional Pairing Originating from the Disconnected Fermi Surfaces of Superconducting LaFeAsO_{1-x}F_x. *Phys. Rev. Lett.* **101**, 087004 (2008).

57. Su-Peng, K. *et al.* Coexistence of itinerant electrons and local moments in iron-based superconductors. *Europhys. Lett.* **88**, 17010 (2009).
58. Hansmann, P. *et al.* Dichotomy between large local and small ordered magnetic moment in Iron-based superconductors. *Phys. Rev. Lett.* **104**, 197002 (2010).
59. Daghofer, M. *et al.* Orbital-weight redistribution triggered by spin order in the pnictides. *Phys. Rev. B* **81**, 180514(R) (2010).
60. Yin, Z. P. and Pickett, W. E. Crystal symmetry and magnetic order in iron pnictides: A tight-binding Wannier function analysis. *Phys. Rev. B* **81**, 174534 (2010).
61. Oh, H. *et al.* Orbital-selective magnetism in FeAs-based superconductors. arXiv: 1012.2224 (2010).
62. Richard, P., Qian, T., and Ding, H. ARPES measurements of the superconducting gap of Fe-based superconductors and their implications to the pairing mechanism. *J. Phys.: Condens. Matter.* **27**, 293203 (2015).
63. Zhang, Y. *et al.* Nodal superconducting-gap structure in ferropnictide superconductor $\text{BaFe}_2(\text{As}_{0.7}\text{P}_{0.3})_2$. *Nat. Phys.* **8**, 371-375 (2012).
64. K. Hashimoto, *et al.* Line nodes in the energy gap of superconducting $\text{BaFe}_2(\text{As}_{1-x}\text{P}_x)_2$ single crystals as seen via penetration depth and thermal conductivity. *Phys. Rev. B* **81**, 220501 (2010).

65. Hashimoto, K. *et al.* Nodal versus Nodeless Behaviors of the Order Parameters of LiFeP and LiFeAs Superconductors from Magnetic Penetration-Depth Measurements. *Phys. Rev. Lett.* **108**, 047003 (2012).
66. Song, C. L. *et al.* Direct Observation of Nodes and Twofold Symmetry in FeSe Superconductor. *Science* **332**, 1410-1413 (2011).
67. Xu, H. C. *et al.* Highly Anisotropic and Twofold Symmetric Superconducting Gap in Nematically Ordered FeSe_{0.93}S_{0.07}. *Phys. Rev. Lett.* **117**, 157003 (2016).
68. Peng, R. *et al.* Enhanced superconductivity and evidence for novel pairing in single-layer FeSe on SrTiO₃ thin film under large tensile strain *Phys. Rev. Lett.* **112**, 107001 (2014).
69. Zhang, Y. *et al.* Superconducting Gap Anisotropy in Monolayer FeSe Thin Film. *Phys. Rev. Lett.* **117**, 117001 (2016).
70. Hoffman, J. E. Spectroscopic scanning tunnelling microscopy insights into Fe-based superconductors. *Rep. Prog. Phys.* **74**, 124513 (2011).
71. Teague, M. L. *et al.* Measurement of a Sign-Changing Two-Gap Superconducting Phase in Electron-Doped Ba(Fe_{1-x}Co_x)₂As₂ Single Crystals Using Scanning Tunneling Spectroscopy. *Phys. Rev. Lett.* **106**, 087004 (2011).
72. Wei, F. *et al.* Evidence for multiple gaps in the specific heat of LiFeAs crystals. *Phys. Rev. B* **81**, 134527 (2010).

73. Johnston, S. *et al.* Specific heat of $\text{Ca}_{0.32}\text{Na}_{0.68}\text{Fe}_2\text{As}_2$ single crystals:
Unconventional s_{\pm} multiband superconductivity with intermediate repulsive interband coupling and sizable attractive intraband couplings. *Phys. Rev. B* **89**, 134507 (2014).
74. Hirschfeld, P. J., Korshunov, M. M., and Mazin, I. I. Gap symmetry and structure of Fe-based superconductors. *Rep. Prog. Phys.* **74**, 124508 (2011).
75. Liu C, *et al.* Importance of the Fermi-surface topology to the superconducting state of the electron-doped pnictide $\text{Ba}(\text{Fe}_{1-x}\text{Co}_x)_2\text{As}_2$. *Phys. Rev. B* **84**, 020509(R) (2011).
76. Ye, Z. R. *et al.* Angle-resolved photoemission spectroscopy study on iron-based superconductors. *Chin. Phys. B* **22**, 087407 (2013).
77. Ye, Z. R. *et al.* Simultaneous emergence of superconductivity, inter-pocket scattering and nematic fluctuation in potassium-coated FeSe superconductor. arXiv:1512.02526 (2015).
78. Shen, X. P. *et al.* Electronic structure of $\text{Ca}_{10}(\text{Pt}_4\text{As}_8)(\text{Fe}_{2-x}\text{Pt}_x\text{As}_2)_5$ with metallic Pt_4As_8 layers: An angle-resolved photoemission spectroscopy study. *Phys. Rev. B* **88**, 115124 (2013).
79. Yu, R., Zhu, J.-X., and Si, Q. Orbital-selective superconductivity, gap anisotropy, and spin resonance excitations in a multiorbital t - J_1 - J_2 model for iron pnictides. *Phys. Rev. B* **89**, 024509 (2014).
80. Kreisel, A. *et al.* Orbital selective pairing and gap structures of iron-based superconductors. *Phys. Rev. B* **95**, 174504 (2016).

81. Hu, J.-P. and Hao, N. S_4 Symmetric Microscopic Model for Iron-Based Superconductors. *Phys. Rev. X* **2**, 021009 (2012).
82. Zhai, H., Wang, F., and Lee, D.-H. Antiferromagnetically driven electronic correlations in iron pnictides and cuprates. *Phys. Rev. B* **80**, 064517 (2009).
83. Lee, C. *et al.* Effect of Structural Parameters on Superconductivity in Fluorine-Free LnFeAsO_{1-y} ($\text{Ln}=\text{La},\text{Nd}$). *J. Phys. Soc. Jpn.* **77**, 083704 (2008).
84. Yi, M. *et al.* Dynamic competition between spin-density wave order and superconductivity in underdoped $\text{Ba}_{1-x}\text{K}_x\text{Fe}_2\text{As}_2$. *Nat. Comm.* **5**, 3711 (2014).
85. Nandi, S. *et al.* Anomalous Suppression of the Orthorhombic Lattice Distortion in Superconducting $\text{Ba}(\text{Fe}_{1-x}\text{Co}_x)_2\text{As}_2$ Single crystals. *Phys. Rev. Lett.* **104**, 057006 (2010).
86. Rotter, M., Hieke, C., and Johrendt, D. Different response of the crystal structure to isoelectronic doping in $\text{BaFe}_2(\text{As}_{1-x}\text{P}_x)_2$ and $(\text{Ba}_{1-x}\text{Sr}_x)\text{Fe}_2\text{As}_2$. *Phys. Rev. B* **82**, 014513 (2010).
87. Xu, N. *et al.* Electronic Band Structure of BaCo_2As_2 : A Fully Doped Ferropnictide Analog with Reduced Electronic Correlations. *Phys. Rev. X* **3**, 011006 (2013).
88. Zhang, Y. *et al.* Orbital characters of bands in the iron-based superconductor $\text{BaFe}_{1.85}\text{Co}_{0.15}\text{As}_2$. *Phys. Rev. B* **83**, 054510 (2011).
89. Sekiba, Y. *et al.* Electronic structure of heavily electron-doped $\text{BaFe}_{1.7}\text{Co}_{0.3}\text{As}_2$ studied by angle-resolved photoemission. *New J. Phys.* **11**, 025020 (2009).

90. Backes, S., Guterding, D., Jeschke, H. O., and Valenti, R. Electronic structure and de Haas–van Alphen frequencies in KFe_2As_2 within LDA+DMFT. *New J. Phys.* **16**, 083025 (2014).
91. Zhang, Y. *et al.* Out-of-Plane Momentum and Symmetry-Dependent Energy Gap of the Pnictide $\text{Ba}_{0.6}\text{K}_{0.4}\text{Fe}_2\text{As}_2$ Superconductor Revealed by Angle-Resolved Photoemission Spectroscopy. *Phys. Rev. Lett.* **105**, 117003 (2010).
92. Nakayama, K. *et al.* Universality of superconducting gaps in overdoped $\text{Ba}_{0.3}\text{K}_{0.7}\text{Fe}_2\text{As}_2$ observed by angle-resolved photoemission spectroscopy. *Phys. Rev. B* **83**, 020501(R) (2011).
93. Yao, Y. X., Schmalian, J., Wang, C. Z., Ho, K. M. and Kotliar, G. Comparative study of the electronic and magnetic properties of BaFe_2As_2 and BaMn_2As_2 using the Gutzwiller approximation. *Phys. Rev. B* **84**, 245112 (2011).
94. Suzuki, H. *et al.* Absence of superconductivity in the hole-doped Fe pnictide $\text{Ba}(\text{Fe}_{1-x}\text{Mn}_x)_2\text{As}_2$: Photoemission and x-ray absorption spectroscopy studies. *Phys. Rev. B* **88**, 100501(R) (2013).
95. Zhou, B. *et al.* Electronic structure of BaNi_2As_2 . *Phys. Rev. B* **83**, 035110 (2011).
96. Terashima, T. *et al.* EuFe_2As_2 under High Pressure: An Antiferromagnetic Bulk Superconductor. *J. Phys. Soc. Jpn.* **78**, 33706 (2009).
97. Ideta, S. *et al.* Electronic structure of BaNi_2P_2 observed by angle-resolved photoemission spectroscopy. *Phys. Rev. B* **89**, 195138 (2014).
98. Diehl, J., Backes, S., Guterding, D., Jeschke, H. O., and Valenti, R., Correlation effects in the tetragonal and collapsed-tetragonal phase of CaFe_2As_2 . *Phys. Rev. B* **90**, 085110 (2014).

99. Dhaka, R. S. *et al.* Dramatic changes in the electronic structure upon transition to the collapsed tetragonal phase in CaFe_2As_2 . *Phys. Rev. B* **89**, 020511(R) (2014).
100. Kreyssig, A., *et al.* Pressure-induced volume-collapsed tetragonal phase of CaFe_2As_2 as seen via neutron scattering. *Phys. Rev. B* **78**, 184517 (2008).
101. Razzoli, E. *et al.* Tuning electronic correlations in transition metal pnictides: Chemistry beyond the valence count. *Phys. Rev. B* **91**, 214502 (2015).
102. Adhikary, G. *et al.* Electronic structure of EuFe_2As_2 . *J. Phys.: Condens. Matter* **25**, 225701 (2013).
103. Zhou, B. *et al.* High-resolution angle-resolved photoemission spectroscopy study of the electronic structure of EuFe_2As_2 . *Phys. Rev. B* **81**, 155124 (2010).
104. Subedi, A., Zhang, L., Singh, D. J., and Du, M. H., Density functional study of FeS, FeSe, and FeTe: Electronic structure, magnetism, phonons, and superconductivity. *Phys. Rev. B* **78**, 134514 (2008).
105. Ieki, E. *et al.* Evolution from incoherent to coherent electronic states and its implications for superconductivity in $\text{FeTe}_{1-x}\text{Se}_x$. *Phys. Rev. B* **89**, 140506(R) (2014).
106. Liu, Z. K. *et al.* Experimental observation of incoherent-coherent crossover and orbital-dependent band renormalization in iron chalcogenide superconductors. *Phys. Rev. B* **92**, 235138 (2015).
107. Yoshida, T. *et al.* Orbital character and electron correlation effects on two- and three-dimensional Fermi surfaces in KFe_2As_2 revealed by angle-resolved photoemission

- spectroscopy. *Front. Phys.* **2**, 1-6 (2014).
108. Guo, J. *et al.* Superconductivity in the iron selenide $K_xFe_2Se_2$ ($0 \leq x \leq 1.0$). *Phys. Rev. B* **82**, 180520 (2010).
109. Nekrasov, I. A., Pchelkina, Z. V., and Sadovskii, M. V., Electronic structure of new LiFeAs high- T_C superconductor. *Jetp Lett.* **88**, 543-545 (2008).
110. Dong, X. *et al.* $(Li_{0.84}Fe_{0.16})OHFe_{0.98}Se$ superconductor: Ion-exchange synthesis of large single-crystal and highly two-dimensional electron properties. *Phys. Rev. B* **92**, 064515 (2015).
111. Niu, X. H. *et al.* Surface electronic structure and isotropic superconducting gap in $(Li_{0.8}Fe_{0.2})OHFeSe$. *Phys. Rev. B* **92**, 060504(R) (2015).
112. Juza, R. and Langer, K. Ternäre Phosphide und Arsenide des Lithiums mit Eisen, Kobalt oder Chrom im Cu_2Sb -Typ. *Zeitschrift fuer Anorganische und Allgemeine Chemie* **361**, 58-73 (1968).
113. Singh, D. J. Electronic structure and doping in $BaFe_2As_2$ and LiFeAs: Density functional calculations. *Phys. Rev. B* **78**, 094511 (2008).
114. Kusakabe, K. and Nakanishi, A. First-principles Study of NaFeAs, NaCoAs, and NaNiAs. *J. Phys. Soc. Jpn.* **78**, 124712 (2009).
115. Wang, G., Zheng, L., Zhang, M., and Yang, Z. Suppression of magnetism in $SrFe_{2-x}Ru_xAs_2$: First-principles calculations. *Phys. Rev. B* **81**, 014521 (2010).
116. Zhang, Y. *et al.* Unusual Doping Dependence of the Electronic Structure and

Coexistence of Spin-Density-Wave and Superconductor Phases in Single

Crystalline $\text{Sr}_{1-x}\text{K}_x\text{Fe}_2\text{As}_2$. *Phys. Rev. Lett.* **102**, 127003 (2009).

Figure Legends

Figure 1: General phase diagram and electronic structure of iron-based superconductors.

(a) General phase diagram of iron-based superconductors. The inset shows the lattice structure of the common Fe-As plane. (b) Lattice and magnetic structure in the symmetry breaking states of iron-based superconductors. (c) LDA calculation of the band dispersion along the Γ -M direction in NaFeAs (adapted from Ref. 30, previously published under CC BY-NC-SA license). Right panel defines the different orbitals and their color-coding used throughout the paper. (d) Illustration of the general Fermi surface topology of an iron-based superconductor.

Figure 2: Trends of orbital-dependent electronic correlations in iron-based superconductors.

(a)-(c) Second energy derivatives of the photoemission spectra images taken along the Γ -M direction in SrFe₂P₂ (measured at 10K at 42.5eV under *s* polarization), NaFeAs (adapted from Ref. 30, previously published under CC BY-NC-SA license), and FeSe_{0.44}Te_{0.56} (adapted from Ref. 16, previously published under CC-BY license), respectively, showing the progression from a phosphide to an arsenide to a chalcogenide. The solid lines and numbers are the band dispersions and corresponding band renormalization factors. The renormalization factors are determined by the ratio between the LDA calculated bandwidth and the experimental one. The experimental bandwidths are illustrated by the color bars to the right side of the images. (d) d_{yz} band renormalization factor as a function of Fe-Pn/Ch bond length (defined by the inset). To remove the electron filling effect, we only include compounds that consist of 6 electrons per

Fe. (e) d_{yz} band renormalization factor as a function of electron filling in $\text{Li}(\text{Fe},\text{Co})\text{As}$ and $(\text{Ba},\text{K})(\text{Fe},\text{Co},\text{Ni})_2\text{As}_2$. The phase diagram of Co and K doped BaFe_2As_2 is also plotted in the background where pink (green) region indicates the superconducting (SDW) phase. (f) d_{yz} band renormalization factor for all available compounds as functions of bond length and electron filling. The color of the markers in (d) and (f) indicates the d_{yz} renormalization factor as shown in the color bar. (g) The renormalization ratio between d_{xy} and d_{yz} bands as a function of the d_{yz} renormalization factor. (h) The renormalization ratio between d_{xy} and d_{yz} bands as a function of bond angle (defined by the inset). (i) Overall plot of the renormalization ratio between d_{xy} and d_{yz} bands for all available compounds as functions of bond angle and the d_{yz} renormalization factor. The color of the markers in (g)-(i) indicates the renormalization ratio between d_{xy} and d_{yz} as shown in the color bar. (See Table 1 for references used in generating (d)-(i).) (Panel a contains unpublished data.)

Figure 3: Renormalization factors against lattice constants. The d_{yz} renormalization factors against lattice constants (a) a and (b) c for undoped compounds. The same for the d_{xy} renormalization factors against lattice constants (c) a and (d) c for undoped compounds. The lattice constant c is adjusted to be per Fe layer for comparison among different structural families by dividing by two for the 122 structures. (See Table 1 for references used in generating all panels.)

Figure 4: Orbital selective Mott phase in iron-based superconductors. (a) d_{xy} band renormalization factor as a function of bond length (defined by the inset). The color of the markers indicates the d_{xy} renormalization factor as shown in the color bar. (See Table 1 for references used.) (b) The spectral weights of d_{xy} and d_{yz} bands as a function of temperature showing the disappearance of the d_{xy} spectral weight while that of the d_{yz} orbital remains finite (adapted from previously published Fig. 5h in ref. 16 under CC-BY license). (c) Theoretically calculated phase diagram of the orbital selective Mott phase (OSMP) as a function of temperature, Coulomb repulsion U , and electron filling. The blue shading indicates the spectral weight of the d_{xy} orbital, and the solid blue lines indicate where the d_{xy} spectral weight drops to zero, marking the boundary of the OSMP. The red line indicates the boundary of a Mott insulating (MI) phase for integer filling (adapted from previously published Fig. 6 of ref. 16 under CC_BY license).

Figure 5: The band splitting and nematic state in iron-based superconductors. (a)

Illustration of the ARPES measurement on a twinned sample, where the beam spot encompasses multiple orthogonal domains. (b) The second derivative photoemission spectra images taken along the a_0 and b_0 directions in detwinned NaFeAs (adapted from Fig. 6 of ref. 31). (c) The second derivative photoemission spectra image taken along the Γ -M direction at 140 and 70 K in 35-layer FeSe film grown on SrTiO₃ (adapted from Fig. 2 of ref. 36). (d) The absolutely band

splitting energy as a function of momentum along Γ -M (adapted from Fig. 3a of ref. 36). (e)

Illustration of the momentum-dependent orbital anisotropy along Γ -M (adapted from Fig. 3c of ref.

36). (f) Temperature-dependent second derivative photoemission spectra images across the M

point of 35-layer FeSe film grown on SrTiO₃ (adapted from Fig. 4b of ref. 36). (g) Illustration of

the band evolution when the system goes through a nematic transition, including the splitting of

d_{xz}/d_{yz} and of d_{xy} (adapted from Fig. 5 of ref. 36).

Figure 6: Fermi surface reconstruction in the magnetic state in iron-based superconductors.

(a) Illustration of the Fermi surface folding in the magnetic state in the 1-Fe BZ where folding

occurs along the AFM direction to induce small Fermi surfaces. (b) and (c) Illustration and

second derivative plots of the folded Γ/M_x point along the AFM and FM directions. (d) and (e)

Illustration and second derivative plots of the folded M_y/Γ' point along the AFM and FM

directions. Data were taken on detwinned BaFe₂As₂ within the SDW state, with photon energies

and in-plane polarizations labeled in white and red, respectively. (Panels b-e contain unpublished

data.)

Tables

Label	Compound	filling	a (Å)	c (Å)	d_{MX} (Å)	θ_2 (°)	W_{yz} (eV)	W_{yz}^{DFT} (eV)	R_{yz}	R_{xy}	R_{xy}/R_{yz}	Refs.
BFA	BaFe ₂ As ₂	6	3.9622	13.001	2.3980	111.41	0.120	0.405	3.50	3.51	1.00	86, 7
BC1.6	Ba(Fe _{0.984} Co _{0.016}) ₂ As ₂	6.016	3.9621	12.9957	2.3985	111.375	0.120	0.404	3.37			86,87
BC2.5	Ba(Fe _{0.975} Co _{0.025}) ₂ As ₂	6.025	3.9621	12.9927	2.3988	111.355	0.116	0.404	3.48			86, 87
BC3.5	Ba(Fe _{0.965} Co _{0.035}) ₂ As ₂	6.035	3.9621	12.9894	2.3991	111.333	0.126	0.403	3.20			86,87
BC4.5	Ba(Fe _{0.955} Co _{0.045}) ₂ As ₂	6.045	3.9620	12.9861	2.3994	111.311	0.128	0.403	3.14			86,87
BC5.6	Ba(Fe _{0.944} Co _{0.056}) ₂ As ₂	6.056	3.9620	12.9825	2.3997	111.286	0.132	0.402	3.05			86,87
BC7	Ba(Fe _{0.93} Co _{0.07}) ₂ As ₂	6.07	3.9619	12.9778	2.4001	111.255	0.130	0.401	3.09			86,87
BC7.5	Ba(Fe _{0.925} Co _{0.075}) ₂ As ₂	6.075	3.9619	12.9762	2.4003	111.244	0.132	0.401	3.04	2.76	0.91	86,87,88
BC15	Ba(Fe _{0.85} Co _{0.15}) ₂ As ₂	6.15	3.9616	12.9513	2.4025	111.079	0.141	0.397	2.82			86,87,89
BCA	BaCo ₂ As ₂	7	3.958	12.67	2.428	109.2	0.250	0.350	1.40	0.980	0.70	87
BK4.2	Ba _{0.958} K _{0.042} Fe ₂ As ₂	5.979	3.9572	13.0362	2.3978	111.213	0.117	0.412	3.52			86,90,84
BK5.5	Ba _{0.945} K _{0.055} Fe ₂ As ₂	5.9725	3.9556	13.047	2.3978	111.152	0.117	0.415	3.54			86,90,84
BK15	Ba _{0.85} K _{0.15} Fe ₂ As ₂	5.925	3.9442	13.1265	2.3974	110.707	0.103	0.431	4.19			86,90,84
BK40	Ba _{0.6} K _{0.4} Fe ₂ As ₂	5.8	3.9141	13.3358	2.3964	109.534	0.102	0.476	4.66			86,90,91
BK70	Ba _{0.3} K _{0.7} Fe ₂ As ₂	5.65	3.8781	13.5869	2.3952	108.127	0.085	0.528	6.22			86,90,92
BM8	Ba(Fe _{0.92} Mn _{0.08}) ₂ As ₂	5.92	3.9781	13.0388	2.4117	111.172	0.111	0.355	3.58			86,93,94
BNA	BaNi ₂ As ₂	8	4.142	11.65	2.405	118.9			1.66			95
BNP	BaNi ₂ P ₂	8	3.947	11.820	2.260	121.71	0.544	0.645	1.18			96,97
BP15	BaFe ₂ (As _{0.85} P _{0.15}) ₂	6	3.9444	12.914	2.3772	112.157	0.125	0.427	3.41	3.25	0.95	86,7
BP20	BaFe ₂ (As _{0.8} P _{0.2}) ₂	6	3.9385	12.885	2.3702	112.406	0.133	0.434	3.26	2.68	0.82	86,7
BP30	BaFe ₂ (As _{0.7} P _{0.3}) ₂	6	3.9266	12.827	2.3563	112.904	0.145	0.449	3.09	2.11	0.68	86,7
BP50	BaFe ₂ (As _{0.5} P _{0.5}) ₂	6	3.9029	12.712	2.3285	113.9	0.171	0.478	2.79	1.81	0.65	86,7
CFA	CaFe ₂ As ₂	6	3.872	11.730	2.370	109.5	0.109	0.338	3.10			98,99
CFAcT	CaFe ₂ As ₂ -cT	6	3.978	5.304	2.34	116.4	0.098	0.281	2.88			100,98,99
CFP	CaFe ₂ P ₂	6	3.855	9.985	2.240	118.74	0.278	0.438	1.57	1.50	0.96	101
EFA	EuFe ₂ As ₂	6	3.9062	12.1247	2.382	110.1	0.098	0.315	3.22			102,103
FS	FeSe	6	3.774	5.523	2.395	104.02	0.140	0.592	4.23			104,32
FTS20	FeTe _{0.80} Se _{0.20}	6	3.8156	6.123	2.5614	96.484	0.089	0.483	5.46			104,105
FTS28	FeTe _{0.72} Se _{0.28}	6	3.8114	6.063	2.545	97.238	0.099	0.494	5.00	22.13	4.42	104,106
FTS30	FeTe _{0.70} Se _{0.30}	6	3.8104	6.048	2.5406	97.426	0.100	0.497	4.97			104,105
FTS35	FeTe _{0.65} Se _{0.35}	6	3.8078	6.0105	2.5302	97.897	0.102	0.503	4.92	18.81	3.82	104,106
FTS40	FeTe _{0.60} Se _{0.40}	6	3.8052	5.973	2.5198	98.368	0.110	0.510	4.64			104,105
FTS45	FeTe _{0.55} Se _{0.45}	6	3.8026	5.9355	2.5094	98.839	0.114	0.517	4.53	16.46	3.64	104,106
FTS59	FeTe _{0.41} Se _{0.59}	6	3.7953	5.8305	2.4803	100.158	0.125	0.536	4.30	14.86	3.45	104,106
KFA	KFe ₂ As ₂	5.5	3.842	13.838	2.394	106.72	0.079	0.581	7.32			90,107
KFS	KFe ₂ Se ₂	6.16	3.9136	14.0367	2.4406	106.6	0.120	0.375	3.13			108,15
LFA	LiFeAs	6	3.7914	6.364	2.421	103.11	0.111	0.400	3.60	4.24	1.18	109,7
LFOHFS	Li _{0.8} Fe _{0.2} OHFeSe	6.1	3.7705	9.215	2.3941	103.90	0.118	0.442	3.75	7.31	1.9 5	110,111
LFP	LaFe ₂ P ₂	6.5	3.841	10.982	2.242	117.841	0.200	0.309	1.54	1.5 0	0.97	101
LC3	LiFe _{0.968} Co _{0.032} As	6.032	3.7903	6.3578	2.4196	103.123	0.121	0.392	3.24			112,113,7
LC9	LiFe _{0.907} Co _{0.093} As	6.093	3.7883	6.3460	2.4179	103.148	0.140	0.384	2.75			112,113,7
LC12	LiFe _{0.877} Co _{0.123} As	6.123	3.7873	6.3401	2.4170	103.16	0.153	0.380	2.49			112,113,7
LC17	LiFe _{0.83} Co _{0.17} As	6.17	3.7857	6.3310	2.4157	103.179	0.175	0.374	2.41	2.23	1.0 4	112,113,7
LC30	LiFe _{0.7} Co _{0.3} As	6.3	3.7814	6.3058	2.4120	103.232	0.239	0.357	1.49	1.60	1.07	112,113,7
LFPO	LaFePO	6	3.941	8.507	2.280	119.62	0.236	0.558	2.37	2.62	1.1 1	6
NFA	NaFeAs	6	3.9448	6.9968	2.4282	108.64	0.128	0.516	4.03	6.98	1.73	114, 7,30
SFA	SrFe ₂ As ₂	6	3.9243	12.3644	2.388	110.5	0.107	0.354	3.32			115,116
SFP	SrFe ₂ P ₂	6	3.825	11.612	2.251	116.4	0.264	0.499	1.89	1.84	0.97	
SK20	Sr _{0.8} K _{0.2} Fe ₂ As ₂	5.9	3.9115	12.6214	2.3892	109.744	0.091	0.400	4.4 0			115,90,116

Table 1: Material details from literature used for the normal state. d_{MX} is the bond length between the transition element ($M = \text{Fe, Co, Ni, Mn}$) and pnictogen/chalcogen ($X = \text{P, As, Se, Te}$).

θ_2 is the two-fold $X-M-X$ bond angle within an M -centered $M \times 4$ tetrahedron. W_{yz} and W_{yz}^{DFT} are the d_{yz} bandwidth of the data and DFT calculations, respectively, taken as the energy range from the band top at the Γ point and the band bottom somewhere between the Γ point and the M point. If the band top is above E_F and hence not observable, a parabolic fitting of the observable parts of the bands around Γ is used to determine the band top position. R_{yz} , the d_{yz} band

renormalization, is determined by the ratio of W_{yz}^{DFT} and W_{yz} . R_{xy} , the d_{xy} band renormalization, is taken as the ratio of the fitted band slope of the most visible section of the LDA-calculated and measured hole-dispersion near Γ . Structural parameters and W_{yz}^{DFT} for intermediate dopings of a material series are linear interpolations of the end members. The structural parameters are taken from Ref. 3 unless other references are given. All measurement info is taken from the normal state spectra to avoid complications from the spin density wave or orthorhombic phase, and taken at $k_z = 0$ wherever possible. Where references are not given, the data come from unpublished data of the authors. Only compounds with sufficiently complete information including ARPES data, LDA calculation, and relevant information such as structural parameter and/or electron filling are included in each plot. Compounds are ordered alphabetically by label.

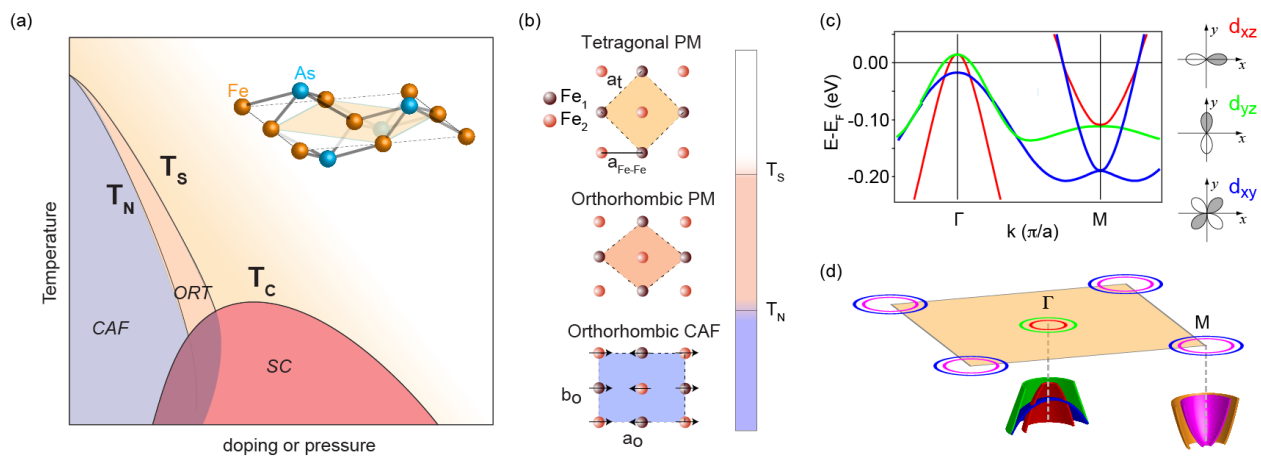


Figure 1

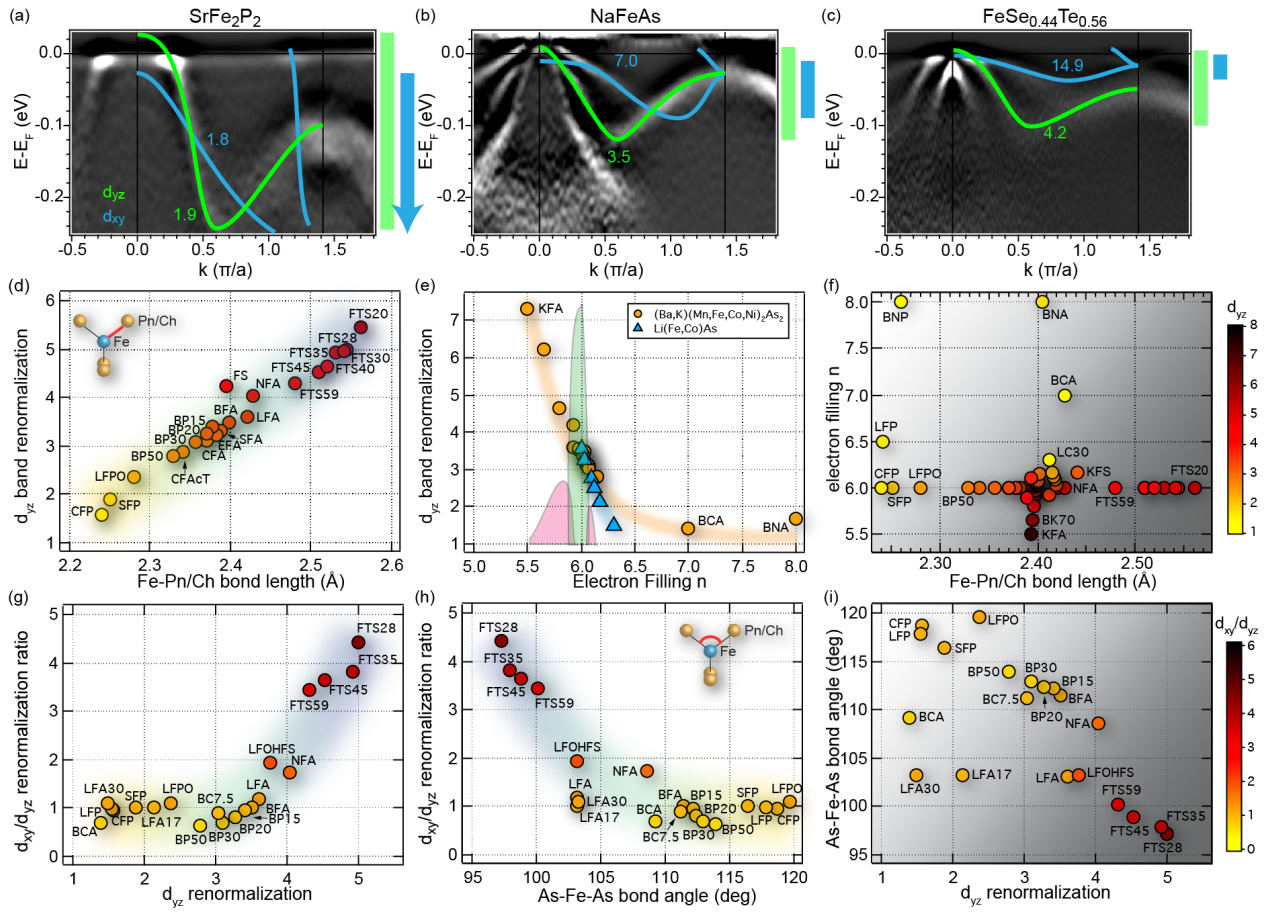


Figure 2

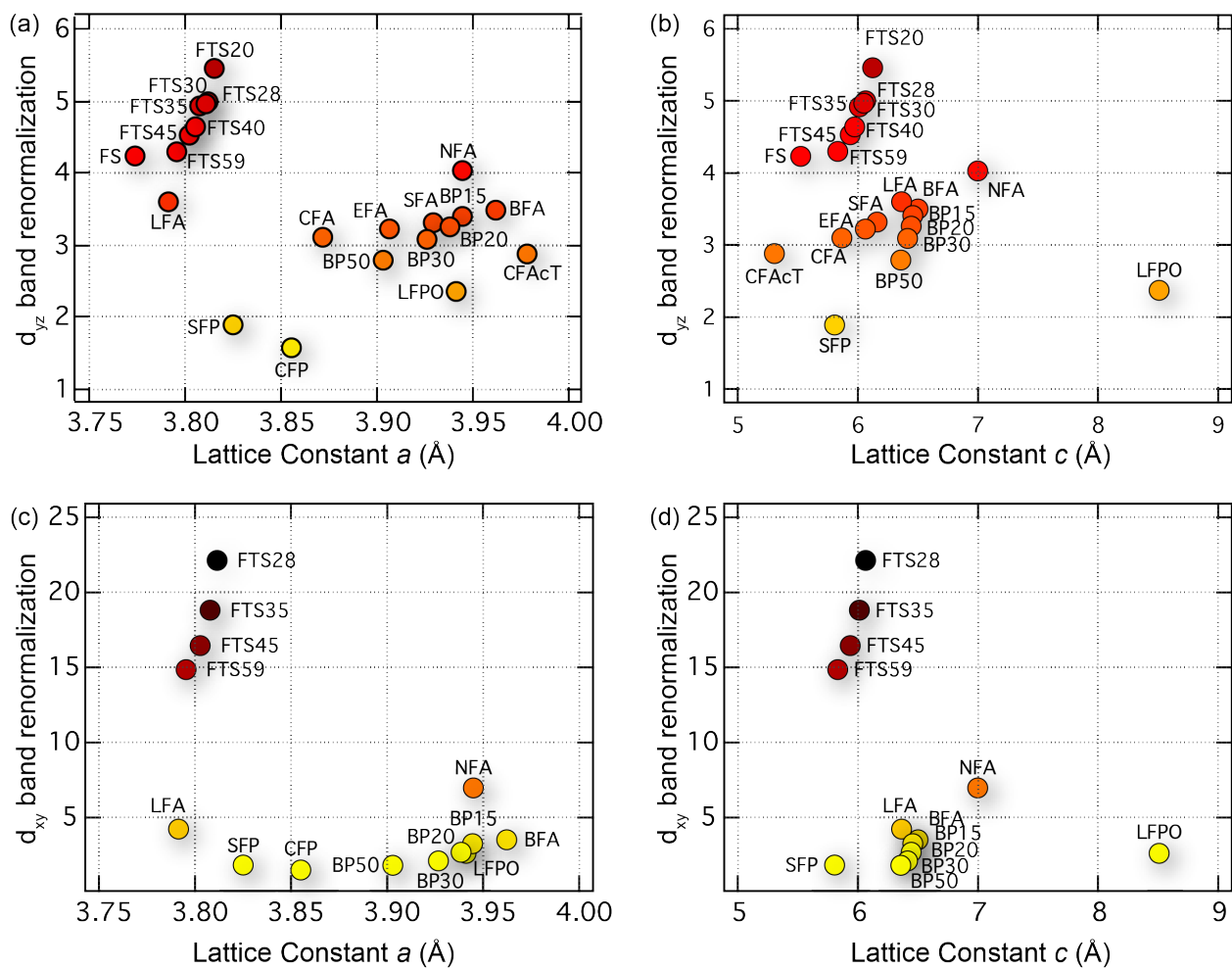


Figure 3

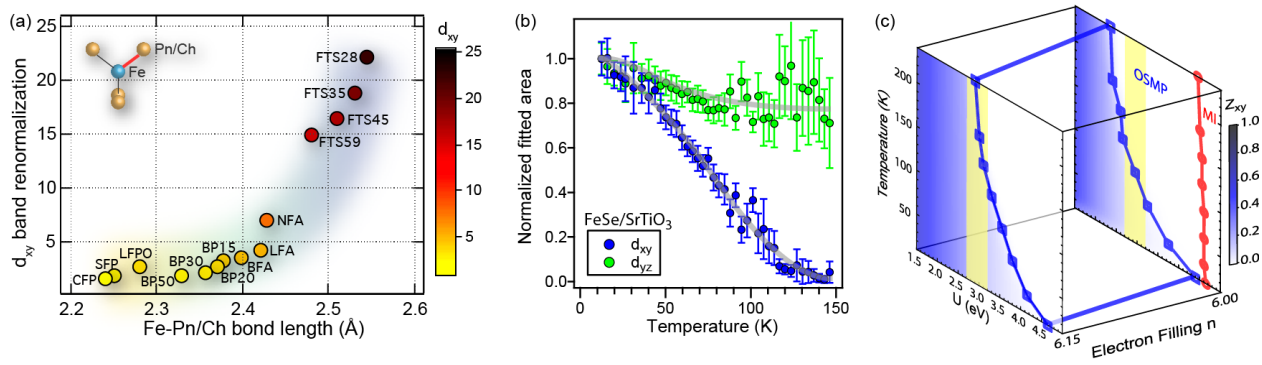


Figure 4

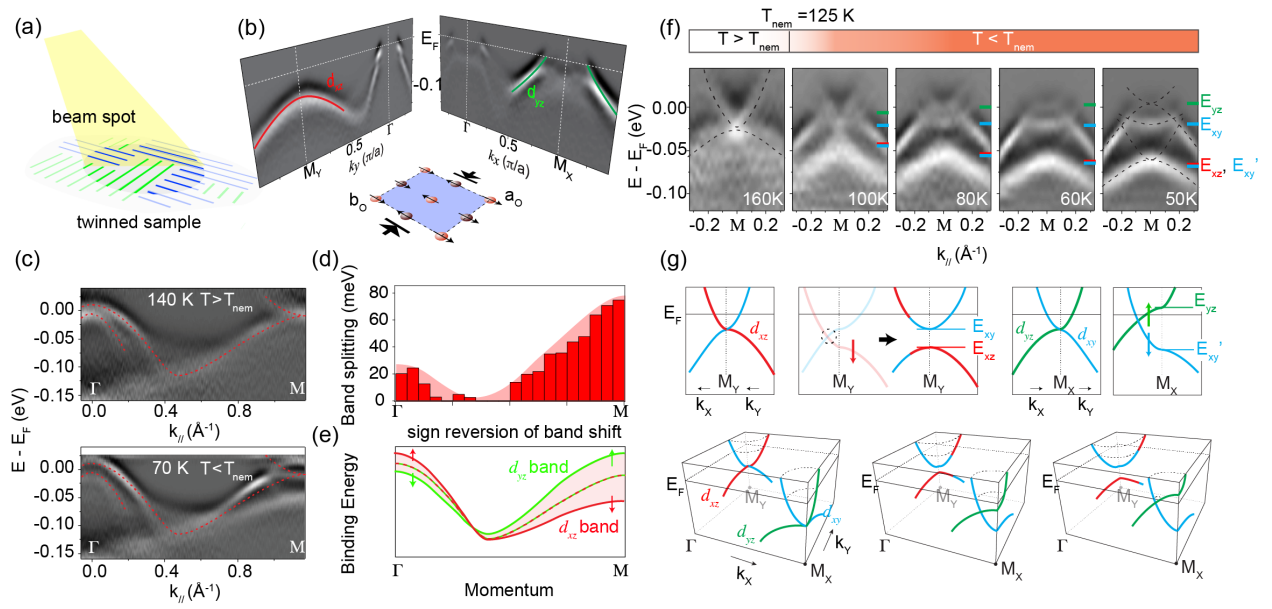


Figure 5

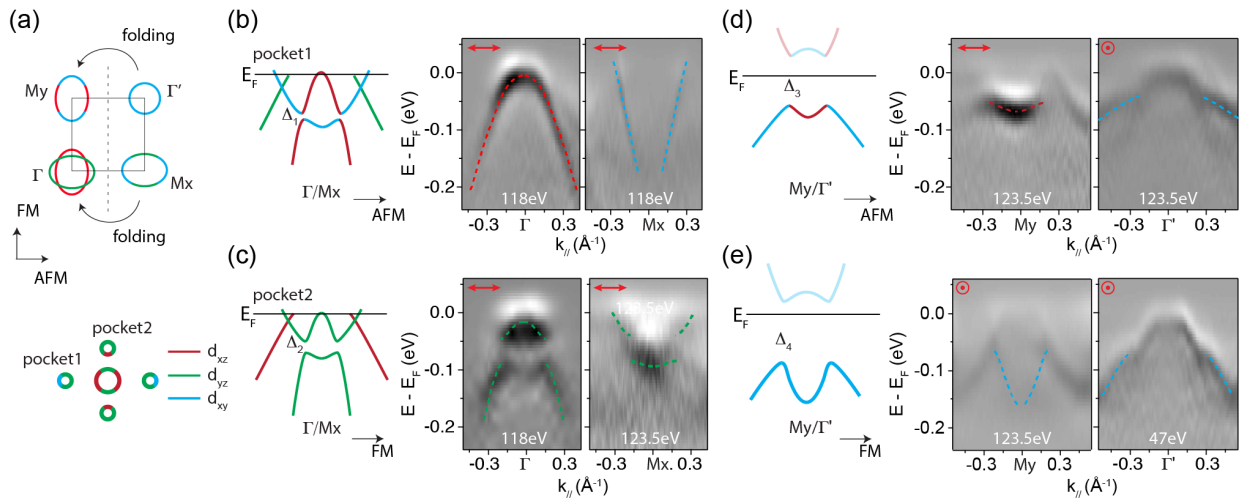


Figure 6